

Near-Simultaneous Hemoglobin Saturation and Oxygen Tension Maps in Mouse Brain Using an AOTF Microscope

Ross D. Shonat,^{*#§} Elliot S. Wachman,^{*} Wen-hua Niu,^{*} Alan P. Koretsky,^{*#§} and Daniel L. Farkas^{*§}

^{*}Center for Light Microscope Imaging and Biotechnology, the [#]Biomedical Engineering Program, and the [§]Department of Biological Sciences, Carnegie Mellon University, 4400 Fifth Avenue, Pittsburgh, Pennsylvania 15213

ABSTRACT A newly developed microscope using acousto-optic tunable filters (AOTFs) was used to generate in vivo hemoglobin saturation (SO₂) and oxygen tension (PO₂) maps in the cerebral cortex of mice. SO₂ maps were generated from the spectral analysis of reflected absorbance images collected at different wavelengths, and PO₂ maps were generated from the phosphorescence lifetimes of an injected palladium-porphyrin compound using a frequency-domain measurement. As the inspiratory O₂ was stepped from hypoxia (10% O₂), through normoxia (21% O₂), to hyperoxia (60% O₂), measured SO₂ and PO₂ levels rose accordingly and predictably throughout. A plot of SO₂ versus PO₂ in different arterial and venous regions of the pial vessels conformed to the sigmoidal shape of the oxygen-hemoglobin dissociation curve, providing further validation of the two mapping procedures. The study demonstrates the versatility of the AOTF microscope for in vivo physiologic investigation, allowing for the generation of nearly simultaneous SO₂ and PO₂ maps in the cerebral cortex, and the frequency-domain detection of phosphorescence lifetimes. This class of study opens up exciting new possibilities for investigating the dynamics of hemoglobin and O₂ binding during functional activation of neuronal tissues.

INTRODUCTION

The brain, lacking a capacity to store energy, requires a constant delivery of O₂ and nutrients to maintain neuronal function. While a detailed understanding of the complex mechanisms employed to regulate this delivery remains elusive, a quantitative measure of the O₂ content in the brain is essential for characterizing the relationship between O₂ and metabolism, and for assessing the ramifications resulting from an inadequate supply. Since the O₂ in blood is either dissolved in plasma or bound to hemoglobin, both the O₂-tension (PO₂) and the O₂-saturation of hemoglobin (SO₂) are important measures of vascular O₂.

Techniques for measuring O₂ in the brain, either directly or indirectly, include the polarographic oxygen electrode (Nair et al., 1975), visible (Watanabe et al., 1994; Malonek and Grinvald, 1996; Bonhoeffer and Grinvald, 1996) and near-infrared reflectance spectroscopy (NIRS) (Jöbsis, 1977; Chance et al., 1988), functional magnetic resonance imaging (f-MRI) (Ogawa et al., 1990, 1992; Kwong et al., 1992), and the oxygen-dependent quenching of injected phosphors (Wilson et al., 1991, 1993; Huang et al., 1994). Of these, NIRS and f-MRI are noninvasive and can be used on humans. While they have become increasingly popular for studying functional activation in the human cortex, the physiologic events underlying the observed signal changes in these noninvasive techniques remains controversial (Jezzard et al., 1994; Menon et al., 1995). Optically based

imaging techniques also are not always directly related to physiologic events, but they do offer a substantially higher spatial and temporal resolution than NIRS or f-MRI. When applied to the study of functional activation in animal models, fundamental biological processes can be probed. In particular, it is important to quantitate the relationship between SO₂ and PO₂ in a variety of physiological conditions.

Reflectance absorbance spectroscopy, which can measure the degree of oxygenation in blood, has been used to monitor cerebral function for many years (Rosenthal et al., 1976; Jöbsis, 1977; Watanabe et al., 1994) and is the basis of NIRS and optical imaging of intrinsic signals. However, because of complicated light scattering and blood volume fluctuations, quantitation of SO₂ in the brain remains problematic. In addition, two-dimensional maps of SO₂ in the cortex have not yet been generated. Recently, Malonek and Grinvald (1996) introduced a microscope capable of generating spatio-spectral images in the cortex. Using a dispersing gradient placed in front of a camera, reflection spectra along an arbitrary line in the cortex were measured. While an elegant approach with high temporal resolution (up to 100 ms), information was restricted to one-dimension and required the collection of two spatio-spectral images to derive any SO₂ information.

Two-dimensional maps of PO₂ have been generated in many different tissues over the last few years, including the cortex of the brain (Wilson et al., 1991, 1993), the heart (Rumsey et al., 1994), the retina of the eye (Shonat et al., 1992a, b), and tumors (Wilson and Cerniglia, 1992). These maps were generated by a phosphorescence lifetime imaging technique, using an oxygen-sensitive palladium-porphyrin compound injected into the systemic vasculature. This compound has been fully characterized, and its use for in vivo PO₂ investigation is well established (Vanderkooi et al., 1987; Wilson et al., 1991; Lo et al., 1996). However, in

Received for publication 3 February 1997 and in final form 2 June 1997.

Address reprint requests to Dr. Daniel L. Farkas, Mellon Institute, 4400 Fifth Avenue, Pittsburgh, PA 15213. Tel.: 412-268-6460; Fax: 412-268-6571; E-mail: farkas@andrew.cmu.edu.

Ross D. Shonat and Elliot S. Wachman made equal contributions to this study.

© 1997 by the Biophysical Society

0006-3495/97/09/1223/09 \$2.00

all applications published to date, the PO_2 maps were generated by a time-domain analysis of the phosphorescence data. Frequency-domain measurements, used in the past for fluorescence lifetime measurements (Lakowicz et al., 1984, 1992), have not as yet been used for phosphorescence lifetime imaging *in vivo*. Although the two techniques provide identical information for simple systems, the frequency-domain approach has broader application to systems with multiple, closely spaced lifetimes (Lakowicz et al., 1984, 1992).

Traditionally, intravital microscopes used for these types of optical imaging experiments are outfitted with wavelength-selective filters and optical elements to measure one particular type of signal, such as fluorescence or reflected light intensity. Multi-mode microscopes have been developed which enable imaging of several different types of signals (Farkas et al., 1993), but these require the use of mechanical switching devices, such as filter wheels, shutters, and port changers. As a result, they are limited in speed as well as spectral flexibility.

Recently, an extension of the multi-mode microscope using acousto-optic tunable filters (AOTFs) for both excitation and imaging has been developed (Wachman et al., 1996, 1997), which provides for fast, versatile multi-modal operation without filter wheels and shutters. In this study, we describe the application of this new intravital AOTF microscope to the generation of both SO_2 and PO_2 maps in the cerebral cortex of mice. Using reflected absorbance spectroscopy through the imaging AOTF, we obtain two-dimensional SO_2 maps. Using a palladium (Pd)-porphyrin compound as an oxygen-sensitive phosphorescent probe

together with intensity modulation of both the excitation and imaging AOTF crystals, we obtain frequency-domain PO_2 maps. Both sets of measurements are made nearly simultaneously, as inspiratory O_2 levels are varied using this single AOTF-based instrument. This versatility opens up the possibility for important new physiologic investigations, including the dynamics of hemoglobin and O_2 -binding during functional activation of neuronal tissues.

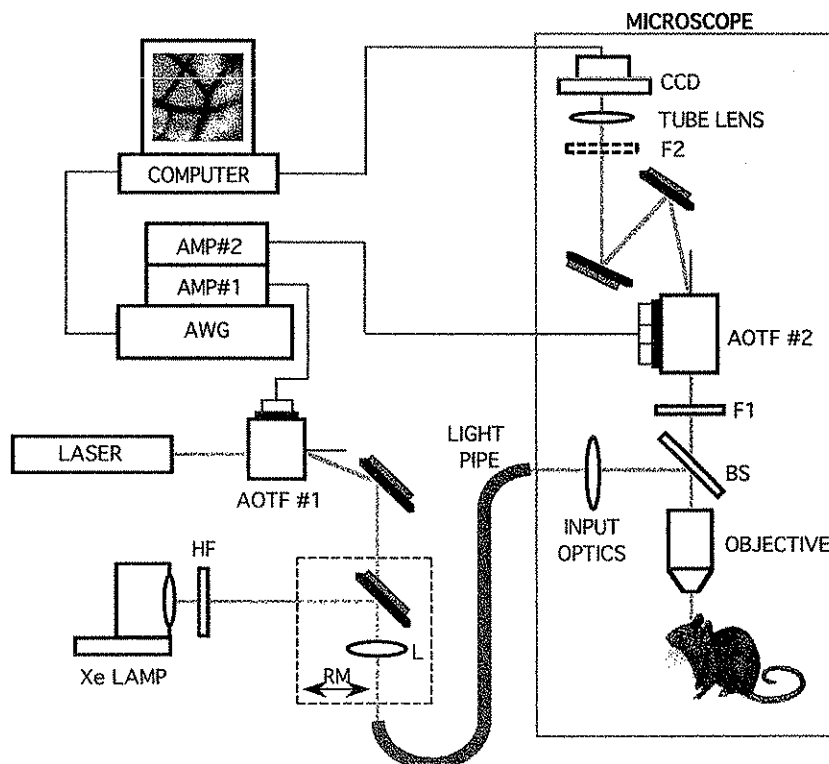
MATERIALS AND METHODS

AOTF microscope

The AOTF microscope shown in Fig. 1 is built around a research-grade fluorescence microscope (Axioplan; Carl Zeiss, Jena, Germany) using two AOTF crystals, and is described in detail elsewhere (Wachman et al., 1997). Two light sources for epi-illumination are used; an argon-krypton gas laser (model Innova 70 Spectrum; Coherent, Santa Clara, CA) modulated by AOTF #1 for phosphorescence lifetime imaging, and a white-light 75-W Xe arc lamp (Carl Zeiss) with heat filter (HF, model 417054; Carl Zeiss) for reflectance imaging. A manually removable mount (RM) selects for the appropriate illumination source. Light entering the microscope through a 2-mm diameter plastic optical fiber (Fiberoptic Engineering, Panama City, FL) is directed onto the tissue via a beam splitter (BS) and an infinity-corrected 10 \times objective (model 440330, NA 0.30; Carl Zeiss). For reflectance measurements, BS is a broadband beam splitter (model XB14-25X36; Omega Optical, Brattleboro, VT); for phosphorescence imaging, BS is a dichroic mirror (572-nm longpass; Omega Optical).

In the emission pathway are two additional filter elements (F1 and F2). For reflectance imaging, F1 and F2 are cross-polarizing filters and for phosphorescence lifetime imaging, F1 is a long-pass filter (645 nm LP; Omega Optical) and F2 is removed. These filters help to compensate for the low background rejection of the imaging AOTF crystal (Wachman et al., 1997). Images are recorded on a cooled CCD slow-scan imaging camera (model PH220; Photometrics, Tucson, AZ) with a Kodak KAF-

FIGURE 1 Schematic representation of the AOTF microscope, showing the major components and light paths for imaging reflected absorbance spectra and phosphorescence lifetimes in the cerebral cortex. AOTF: acousto-optic tunable filter; AWG: arbitrary waveform generator; BS: beam splitter; F1 and F2: filter elements; HF: heat filter; L: lens; RM: removable mount. Optical elements not present in certain experiments are indicated by dashed lines.



1400 chip (1317 × 1035 array of 6.8 × 6.8 μm pixels) mounted behind AOTF #2 and controlled by a Macintosh Quadra 950 computer. To increase the signal-to-noise, 6 × 6 binning of the CCD chip is used. For the 10× objective, each binned pixel collects light from a 4 × 4 μm region. All images are digitized and stored on the same computer for subsequent processing and map generation.

Electronic control of the AOTF crystals is provided by two broadband RF amplifiers (NEOS Technologies, Melbourne, FL), controlled by a two-channel 400-MHz arbitrary waveform generator (AWG, model LW420; LeCroy, Chestnut Ridge, NY).

Reflectance absorbance spectroscopy of hemoglobin

The absorbance spectra of hemoglobin changes upon binding O₂, therefore a spectral decomposition of the reflected absorbance signal arising from white light illumination can be used to calculate SO₂. In particular, since deoxy- and oxy-hemoglobin (Hb and HbO₂) are the dominant light-absorbing molecules in blood between 500 and 600 nm, the absorbance, *Abs*, at a specified wavelength λ can be approximated, by extension of the Beer-Lambert law, as

$$Abs_{\lambda} = -\log(I_{\lambda}/I_{\lambda}^0) = (\epsilon_{\lambda}^{HbO_2}[HbO_2] + \epsilon_{\lambda}^{Hb}[Hb])L + LS, \quad (1)$$

where I_{λ} and I_{λ}^0 are the measured light intensities in the presence and absence of hemoglobin, $\epsilon_{\lambda}^{HbO_2}$ and ϵ_{λ}^{Hb} are the textbook extinction coefficients for HbO₂ and Hb, $[HbO_2]$ and $[Hb]$ are the concentrations of HbO₂ and Hb, L is the optical path length, and LS is a composite light-scattering term (taken here as wavelength-independent) (Malonek and Grinvald, 1996). For in vivo studies, I_{λ}^0 can be approximated by the average reflected intensity from a region void of pial vessels and corrects for variations in the spectral response of the illumination and detection optical systems. If the total hemoglobin concentration, $[Hb_T] = ([HbO_2] + [Hb])$, is arbitrarily assigned a value of 1, then there are three unknown parameters in Eq. 1, $[HbO_2]$ (or $[Hb]$), L , and LS . These unknowns can be found by the method of least squares from Abs_{λ} measurements taken at a number of different wavelengths, with SO₂ then given by $[HbO_2]$, the percentage of total O₂-bound hemoglobin. The coefficient of determination, R^2 , may be calculated from the least-squares analysis and used to reject pixels that cannot be fit accurately.

Generation of SO₂ maps by reflectance imaging of hemoglobin spectra

For the absorbance spectra measurements using white light illumination with the Xe lamp, an image exposure time of 2 s was used, corresponding to a total light energy density delivered to the tissue per exposure of ~70 mJ/cm². Thirteen images were acquired and transferred to the computer as AOTF #2 was rapidly varied from 504 to 600 nm (bandwidth = 5 nm) in 8-nm increments. It took ~75 s to acquire the image set.

Oxygen-sensitive phosphorescent probe

The palladium porphyrin derivative, Pd *meso*-tetra [4-carboxyphenyl] porphyrine (Porphyrin Products, Logan, UT), when bound to albumin and injected into the systemic vasculature, has been shown to be a sensitive and accurate indicator of blood PO₂ (Vanderkooi et al., 1987; Wilson et al., 1991; Lo et al., 1996; Shonat and Johnson, 1997). Because O₂ is a powerful quenching agent and the only significant one in blood (Wilson et al., 1991), the phosphorescence lifetime of this probe, τ (μs), is inversely proportional to PO₂ according to the Stern-Volmer equation

$$\tau_0/\tau = 1 + k_Q\tau_0PO_2, \quad (2)$$

where τ_0 (μs) is the lifetime in the absence of O₂ and k_Q (mmHg⁻¹ s⁻¹) is the bimolecular rate, or quenching, constant. The constants k_Q and τ_0 have

been experimentally determined elsewhere (Lo et al., 1996) and apply to in vivo experiments at a given temperature and pH. The probe has two primary peaks in its absorbance spectra (420 and 530 nm) and its phosphorescence emission spectra shows a maximum near 700 nm (Vanderkooi et al., 1987).

Phosphorescence lifetimes by frequency-resolved, phase-sensitive spectroscopy

As described in detail elsewhere (Lakowicz et al., 1992), a phase-sensitive measure of fluorescence or phosphorescence lifetime is possible when 1) the delivered excitation light and the sensitivity of the collection system can be independently modulated, and 2) the phase relationship between these two modulators accurately varied. Typically, a controllable light source power supply and an image intensifier are used as modulators. In our microscope, the two AOTF crystals are used to carry out these functions.

When the probe is excited by light that has been sinusoidally modulated by the excitation AOTF at a circular frequency ω , the phosphorescence emitted will have the same frequency ω , but will be delayed in phase by an angle θ , and demodulated relative to the excitation by a factor m . If the throughput of the emission AOTF when tuned to the phosphorescence maximum is also modulated at ω , but delayed in phase relative to the excitation AOTF by an angle θ_D , the intensity reaching the camera is

$$I(\theta_D) = k[Pd](1 + \frac{1}{2}m_D m \cos\{\theta - \theta_D\}), \quad (3)$$

where k is a constant, $[Pd]$ is the concentration of the probe and m_D is the modulation of the emission AOTF. θ is related to the apparent phase lifetime τ_{θ} by

$$\tan \theta = \omega\tau_{\theta} \quad (4)$$

and m is related to the apparent modulation lifetime τ_m by

$$m = (1 + \omega^2\tau_m^2)^{-1/2}. \quad (5)$$

For a single exponential decay, such as for Pd-porphyrins, $\tau_{\theta} = \tau_m = \tau$ (Lakowicz et al., 1992). Because Eq. 3 contains three unknowns, $k[Pd]$, m , and θ , it is necessary to collect images for various θ_D , and then fit the data to Eq. 3 to determine both θ and m .

Since Eq. 3 is nonlinear, applying it on a pixel-by-pixel basis to the set of images is computationally difficult. Following Lakowicz et al. (1992), we use a linearized form,

$$I(\theta_D) = a_0 + a_1 \cos \theta_D + b_1 \sin \theta_D, \quad (6)$$

where θ and m can be determined by the evaluation of a_0 , a_1 , and b_1 using matrix algebra. Further details of this approach may be found in that paper. PO₂ maps were generated from maps of θ and m using Eq. 4 or 5, respectively, and the Stern-Volmer equation (Eq. 2). A map of R^2 was also generated to reject those pixels below a specified threshold.

Finally, for an accurate determination of θ and m , ω must be selected in accordance with the lifetime of the fluorophore or phosphor. For fluorescence, with τ values typically measured in nanoseconds, modulation frequencies in the MHz range are used. However, for the phosphorescent probe used in this study, with a τ measured in the hundreds of microseconds, maximum in vivo sensitivity is achieved when ω is near 6000 rad/s.

Generation of PO₂ maps by phosphorescence lifetime imaging

For Pd-porphyrin probe excitation, the laser's Ar⁺ line at 514 nm was used. This light was ~95% modulated by AOTF #1 at a linear frequency $f = 1000$ Hz ($\omega = 6283$ rad/s). Exposure time for these measurements was 2 s, with a total delivered light energy density per exposure of ~120 mJ/cm². AOTF #2 was driven with 4 RF frequencies to provide a bandpass of ~25

nm centered at 700 nm. Its throughput was $\sim 40\%$ modulated, also at $f = 1000$ Hz, but was shifted in phase relative to AOTF #1 by θ_D . Eight phosphorescence intensity images were acquired and transferred to the computer as θ_D was varied from 0 to 420° in 60° increments. It took ~ 70 s to acquire the image set. A fluorescence standard, Cy3 (Mujumdar et al., 1993), which has a fast lifetime and a negligible phase shift at the modulation frequencies used for phosphorescence measurements, was used to determine the instrumental phase. This phase error of 4.5° was used to transform all measured phase shifts into actual phase shifts.

Animals and experimental procedures

Mice of different strains and sex were anesthetized with an injection of 2.5% Avertin (0.015 ml/g, IP) and tracheotomized. After a topical anesthetic (1% mepivacaine, 0.05 ml, sc) was injected under the scalp, a clamp was attached between the nasal and palatine bones to immobilize the skull and permit free access to the entire dorsal surface of the cranium. The skull was then exposed and the bone cleaned. Using a dental drill (Foredom, Bethel, CT) with a 1-mm circular drill bit (Stoelting, Wood Dale, IL), a region of the parietal bone caudal to the coronal suture was thinned and carefully removed, leaving the dura intact. A well of petroleum jelly (Vaseline) was built around the exposed cortex, filled with normal saline, and sealed with a coverslip.

The probe was dissolved in a solution (10 mg/ml) with BSA (60 mg/ml, Fraction V, ICN Biochemicals, Costa Mesa, CA) and physiologic saline buffered to a pH of 7.4 and injected (15 mg/kg) into the femoral vein by venous puncture. Systemic equilibration of this probe occurred rapidly (5–10 min). Throughout the procedure, rectal temperature was regulated at 38°C using a water-filled heating blanket and anesthesia was maintained with intraperitoneal injections of urethane (0.75 mg/g) and α -chloralose (0.05 mg/g) as needed. The inspiratory oxygen fraction ($F_{\text{I}}\text{O}_2$) was varied by passing different humidified O_2/N_2 gas mixtures across the tracheal cannula.

After placing the animal on the microscope stage, a region of the exposed cortex having at least one pial artery and vein within the camera's field of view was selected. At an $F_{\text{I}}\text{O}_2$ of 21%, the phosphorescence intensity image series was acquired, followed by the reflected intensity image series. Between the two measurements, it was only necessary to manually switch the excitation light source (by moving RM) and the three optical elements (BS, F1, and F2), since AOTF control and image acquisition was completely automated (see Fig. 1). This procedure was then repeated, in sequence, for an $F_{\text{I}}\text{O}_2$ of 60 and 10%. Three minutes at each $F_{\text{I}}\text{O}_2$ was allowed for physiologic equilibration.

In vitro calibration of the PO_2 measurement

To insure the accuracy of the AOTF microscope for the phosphorescence-based PO_2 measurements, an in vitro calibration was done. Pd *meso*-tetra [4-carboxyphenyl] porphine was dissolved (100 μM) in a physiologic saline solution at pH 7.4 containing BSA (500 μM) and pushed through a 1-mm square capillary tube (model 8110; VitroCom, Mountain Lakes, NJ) at 0.5 ml/min using a peristaltic pump (MasterFlex; Cole-Parmer, Chicago, IL). Two Clark-type oxygen electrodes (model 5331, YSI, Yellow Springs, OH), placed in the fluid stream on either side of the capillary tube were used to measure the PO_2 , and a home-built oxygenator, placed upstream of the capillary tube, allowed for fluid PO_2 changes. Using the procedures outlined above, PO_2 in the capillary tube was measured at room temperature with the AOTF microscope as the O_2 content passing through the oxygenator was changed. The quenching constants for pH 7.4 and 23°C were used ($k_Q = 259 \text{ mmHg}^{-1} \text{ s}^{-1}$, $\tau_0 = 711 \mu\text{s}$) (Lo et al., 1996).

The correspondence of the PO_2 measured by the AOTF microscope and the oxygen electrode is shown in Fig. 2. The slope of a best fit line (dashed) was 0.87 ± 0.06 ($R^2 = 0.94$) and was not significantly different ($p > 0.05$, two-tailed Student's *t*-test) from the line of equality (solid line). While decreases in the overall phosphorescence intensity and increases in the insensitivity of θ to PO_2 at higher O_2 levels contribute to larger errors in the

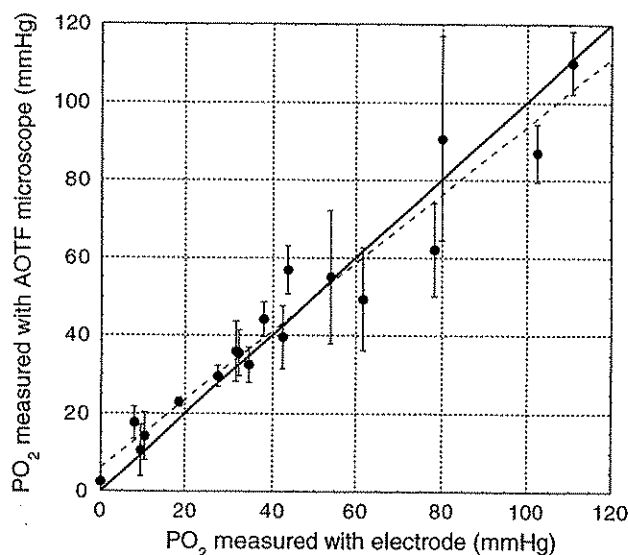


FIGURE 2 In vitro calibration of Pd *meso*-tetra [4-carboxyphenyl] porphine. The PO_2 calculated from the analysis of phosphorescence phase θ using the AOTF microscope is plotted as a function of the measured PO_2 from an oxygen electrode using the calibration system described in Materials and Methods. Errors bars indicate standard deviation. The line of equality (solid) and a least-squares regression line (dashed) are also shown.

phase measurement at higher PO_2 levels, broad agreement between the two methods is demonstrated.

RESULTS

SO_2 and PO_2 measurements

A reflected light image at $\lambda = 560$ nm from the right parietal cortex of one mouse is shown for 10% $F_{\text{I}}\text{O}_2$ in Fig. 3 *a*. Two large pial vessels, one artery (A) and one vein (V), are clearly visible against the whitish background of the cortical tissue. Although not clearly discernible from this image, the artery passes over the vein. In *panel b* of this figure, the corresponding phosphorescence intensity image at $\theta_D = 300^\circ$ ($F_{\text{I}}\text{O}_2 = 10\%$) is shown. The vessels are clearly seen here because the probe density, and the corresponding phosphorescence, are higher than background. The background phosphorescence, arising primarily from the capillaries and smaller vessels below the spatial resolution of the microscope at this magnification, is at or near the limit of detectability. In the two regions where the artery passes over the vein, the phosphorescence intensity is less than in the adjoining region of the vein, indicating that the excitation light did not completely reach the vein. The higher overall intensity in the vein is due both to the larger diameter of this vessel and its lower average PO_2 , since intensity and PO_2 are inversely related (Rumsey et al., 1988).

In the lower two panels of Fig. 3, the fitting of reflected absorbance spectra (*c*) and phosphorescence phase shift (*d*) data are shown for two selected regions: one in the artery (A) and one in the vein (V). Data shown are averages taken

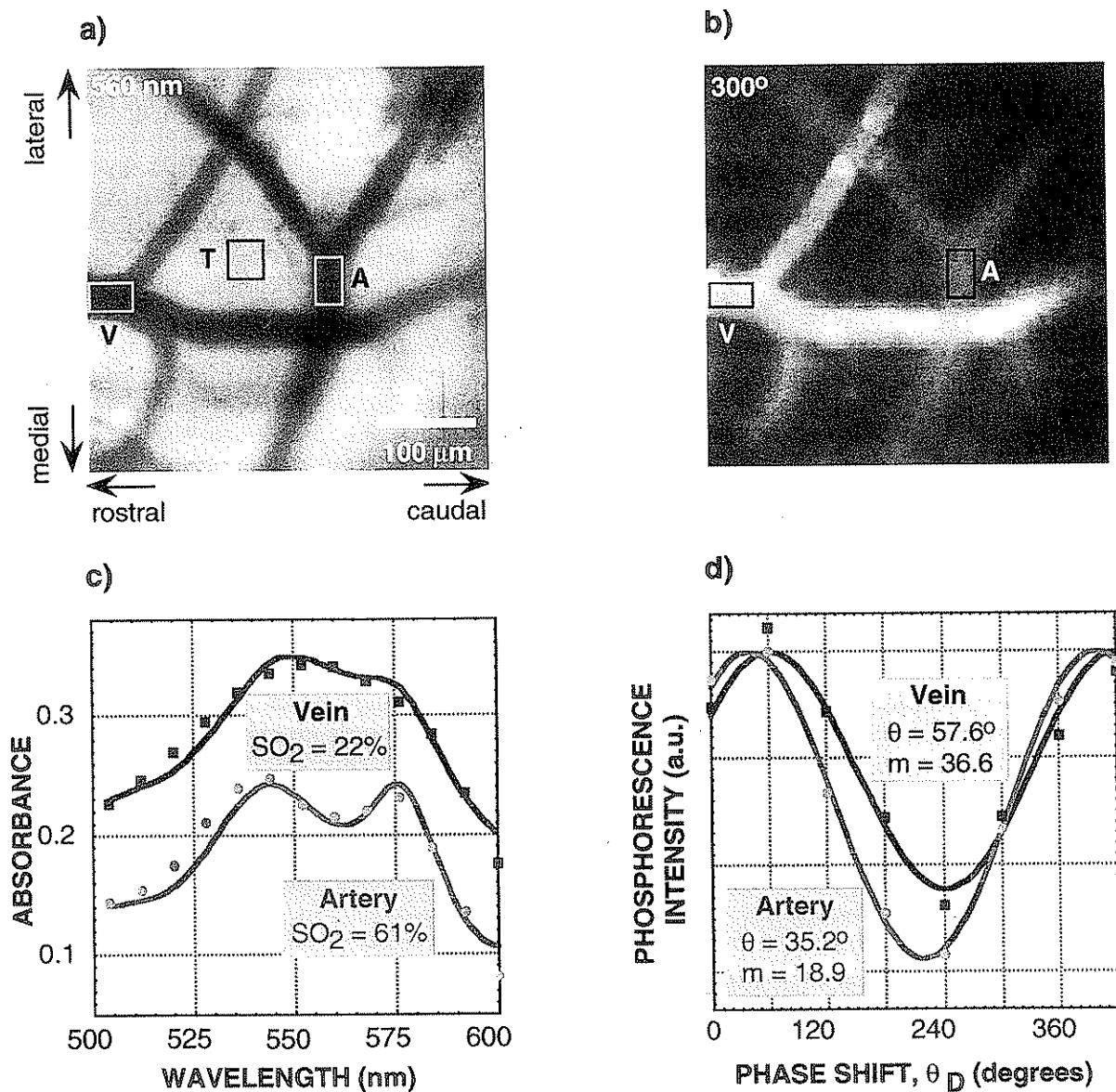


FIGURE 3 Principles of reflectance absorbance and frequency-domain phosphorescence lifetime imaging. (a) Reflected image of the mouse cortex at 560 nm. The three rectangles labeled A, V, and T indicate regions from the artery, vein, and tissue, respectively. (b) Phosphorescence intensity image at $\theta_D = 300^\circ$. (c) Best-fit spectra (lines) and reflected absorbance data for the A (circles) and V (squares) regions. SO_2 is calculated from parametric estimates of $[HbO_2]$ and is shown in the boxed legends. The reflected intensity in T was used for normalization. (d) Best-fit cosine (lines) and phosphorescence intensity data for the A (circles) and V (squares) regions. The parametric estimates of θ and m are shown in the box legends.

over all the pixels in the regions indicated; an analogous procedure is used to obtain the pixel-by-pixel maps of both SO_2 and PO_2 shown below. In Fig. 3 c, the reflected absorbance spectrum of the artery (circles) is clearly distinct from the venous spectrum and displays more of the two-peak character that is representative of an HbO_2 spectrum; SO_2 in this arterial region is $61 \pm 12\%$. By contrast, more of the single-peak character of an Hb spectrum is evident in the venous spectrum, where O_2 is lower ($SO_2 = 22 \pm 10\%$). In both spectra, the region T in Fig. 3 a was used for calculating I_λ^0 . The best-fit spectra for both regions show good agreement to data (arterial $R^2 = 0.86$, venous $R^2 =$

0.87), indicating that the assumptions of Eq. 1 and the I_λ^0 calculation are reasonable.

For the phosphorescence analysis (Fig. 3 d), the calculated phase for the artery ($\theta = 35.2 \pm 8.5^\circ$) is less than that for the vein ($\theta = 57.6 \pm 5.0^\circ$). This is seen clearly by observing that the best-fit sinusoidal curve for the artery (circles) is shifted to the left along the θ_D axis. PO_2 is calculated to be 22.1 ± 2.8 for the artery and 8.0 ± 1.4 for the vein. Because the average phosphorescence intensity in the vein is substantially higher than in the corresponding artery, the ordinate axis in Fig. 3 d is scaled separately for each data set, so that the phase difference between them is

more clearly visible. Modulation values for these data before scaling are shown for both artery ($m = 18.9 \pm 6.0$) and vein ($m = 36.6 \pm 5.0$). As with the reflected absorbance fits, these best-fit sinusoidal curves show good agreement to data (arterial $R^2 = 0.91$, venous $R^2 = 0.94$).

While both phase θ and modulation m were available for generating PO_2 maps, we found that in general those generated from the m data were of much poorer quality. This was especially noticeable at higher O_2 levels, where the phosphorescence signal is lower. Therefore, while θ and m are equivalent indicators of PO_2 for Pd-porphyrins, only θ -generated PO_2 maps are displayed and used in this study.

SO_2 and PO_2 during F_{iO_2} adjustments

Maps of SO_2 and PO_2 are shown in Fig. 4 for 10, 21, and 60% F_{iO_2} . In all maps, pixels with an $R^2 < 0.75$ were assigned the color black. For the SO_2 maps, where low absorbance and our use of a region for calculation of I_{λ}^0 prevented the determination of capillary SO_2 , only the ves-

sels have color. For the PO_2 maps, there is some indication of capillary PO_2 , especially in the 10% map, but in general, the weak phosphorescence signal from these small vessels made accurate fitting difficult and many pixels have been blanked.

From the maps of Fig. 4, SO_2 and PO_2 are seen to increase predictably as the F_{iO_2} is stepped from hypoxia (10% O_2), through normoxia (21% O_2), to hyperoxia (60% O_2). The artery and vein are clearly distinct in both the SO_2 and PO_2 maps, as expected. At an F_{iO_2} of 21%, the pial artery has an SO_2 near 80% and a PO_2 near 40 mmHg. The corresponding pial vein has an SO_2 near 30% and a PO_2 near 20 mmHg. When the F_{iO_2} is stepped to 60% O_2 , an approximate doubling of the SO_2 and PO_2 in the vein is observed (SO_2 to near 60% and PO_2 to near 40 mmHg). However, while the PO_2 in the artery increases to near 60 mmHg, the SO_2 increases only slightly, indicating that hemoglobin is close to saturation. With an F_{iO_2} of 10%, SO_2 and PO_2 levels are dramatically lower: SO_2 is near 50% in the artery and 20% in the vein, PO_2 is below 30 mmHg

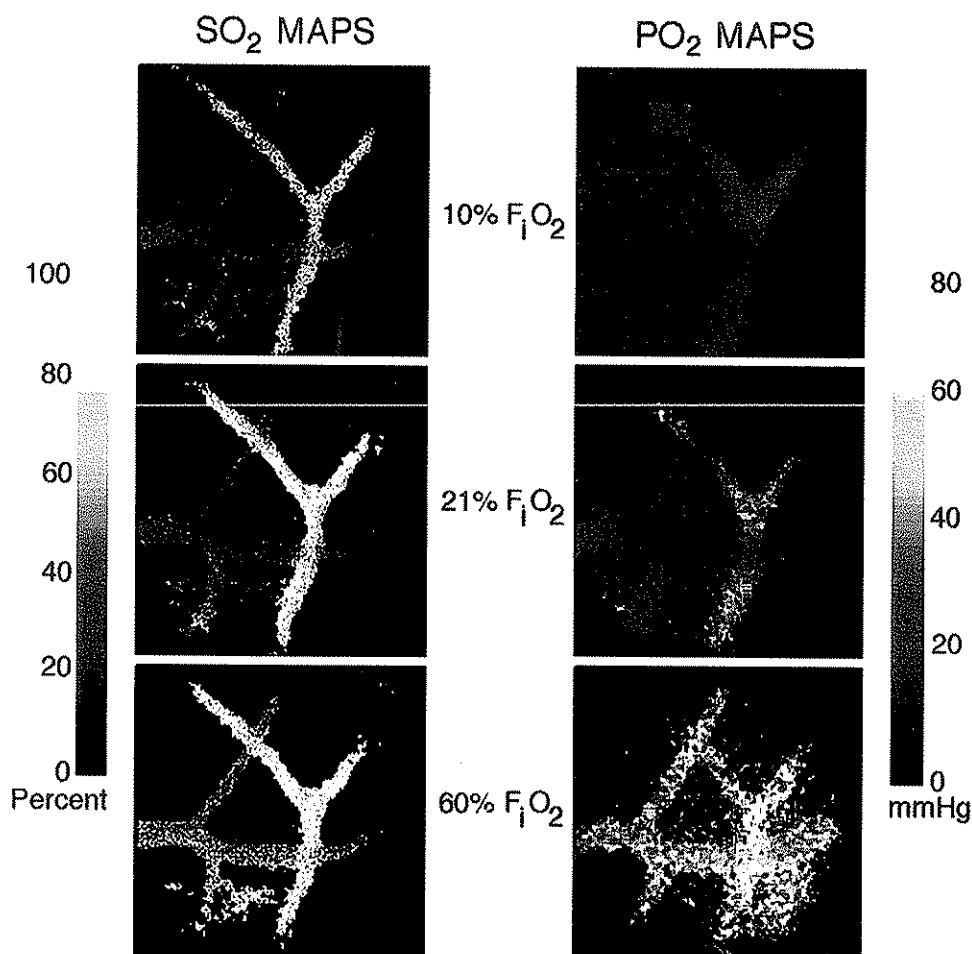


FIGURE 4 Maps of SO_2 and PO_2 at steady state in the cerebral cortex at 10, 21, and 60% F_{iO_2} using the procedures described in Materials and Methods. Pixels with $R^2 < 0.75$ in all maps were masked to black. As F_{iO_2} was stepped from hypoxia (10% O_2), through normoxia (21% O_2), to hyperoxia (60% O_2), SO_2 and PO_2 levels rose accordingly and predictably throughout. The artery, containing more oxygen than the vein, is clearly distinguishable by color in both the SO_2 and PO_2 maps.

in the artery and 10 mmHg in the vein. While a PO₂ measurement was not always possible in regions surrounding the pial vessels, especially at the two higher F_iO₂ levels, capillary PO₂ at 10% F_iO₂ is between 10 and 20 mmHg and is clearly higher than in the overlying vein.

Since the relationship between SO₂ and PO₂ is defined by an oxygen-hemoglobin dissociation curve, we show in Fig. 5 a plot of SO₂ data versus PO₂ data for 19 cortical regions in 15 mice. For arteries (*circles*) and veins (*squares*), the averaged SO₂ is plotted as a function of the averaged PO₂ at different F_iO₂ levels. The solid curve in this figure is the hemoglobin dissociation curve for the C57BL/6J mouse strain (Fabry et al., 1992) with a PO₂ at 50% saturation (p50) equal to 41.5 mmHg, and the dashed curve is a best-fit of the data to the Adair equation (Adair, 1925). The Adair equation is based on a theoretical model for the allosteric binding of oxygen to hemoglobin, and the calculated p50 for this fit curve is 50 mmHg. Because the quantity of O₂ bound to hemoglobin does not increase linearly with increasing PO₂, but rather shows a sigmoidal shape common for systems displaying an allosteric interaction, one would expect that a direct comparison between the SO₂ and PO₂ maps would also have this sigmoidal character. Despite the variability of the data, the results shown in Fig. 5 are indicative of this general shape. Most of the data points lie to the right of the published dissociation curve for the C57BL/6J mouse strain, giving rise to a best-fit dissociation curve, which is right-shifted.

DISCUSSION

The principal aims of the present investigation were: 1) to generate 2-D maps of cerebral vascular SO₂, 2) to apply a

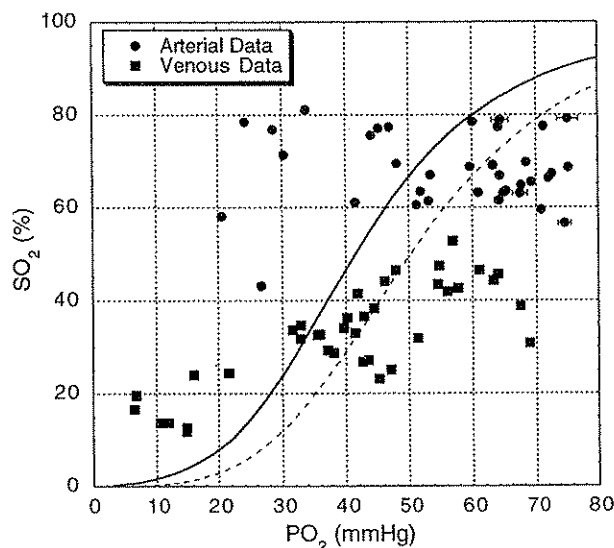


FIGURE 5 Comparison of the SO₂ and PO₂ data for 19 cortical regions in 15 mice to the oxygen-hemoglobin dissociation curve for the C57BL/6J mouse strain (Fabry et al., 1992) (*solid curve*) and the best fit ($R^2 = 0.58$) of the data to the Adair equation (Adair, 1925) (*dashed curve*). Separate arterial regions (*circles*) and venous regions (*squares*) were used to generate the data shown. Error bars indicate standard error of the mean.

frequency-domain technique to the generation of PO₂ maps in the cortex using an oxygen-sensitive phosphorescent probe, and 3) to map SO₂ and PO₂ at various O₂-levels with a single instrument, the AOTF microscope.

The SO₂ maps in this study were generated by a spectral decomposition of the reflected absorbance signal arising from white light illumination. In defining Abs_{λ} (Eq. 1), we assumed that only two light-absorbing molecules, Hb and HbO₂, were present in blood. Because the Pd-porphyrin concentration ($\sim 400 \mu\text{M}$) was $<20\%$ of the hemoglobin concentration ($\sim 2.2 \text{ mM}$), its spectral absorbance was ignored. We also assumed that the light scattering term, LS , was not wavelength-dependent. Making LS dependent on wavelength, such as a λ^4 -dependency used by others (Watanabe et al., 1994; Malonek and Grinvald, 1996), had little effect on the fits or resulting SO₂ calculation. Finally, we assumed that the background reflected intensity, I_{λ}^0 , from a nearby tissue region could be used as an accurate measure of the reflected intensity without hemoglobin. Some groups have used an artificial reflecting surface placed next to the tissue (Sato et al., 1979; Watanabe et al., 1994) and/or adjusted the extinction coefficients for HbO₂ and Hb to account for complicated scattering in tissue (Watanabe et al., 1994). Others have used the difference between two spectra to eliminate the I_{λ}^0 term; this is the basis of optical spectroscopy using intrinsic signals (Malonek and Grinvald, 1996; Bonhoeffer and Grinvald, 1996). This latter technique, however, cannot be used to generate SO₂ maps from a single spectral image series. Our choice of determining I_{λ}^0 from the reflected intensity measured from a surrounding tissue region (region T from Fig. 3 a) is simpler than the above techniques, but assumes that the hemoglobin concentration in the surrounding region is substantially less than in the pial vessels, and that the reflectance is approximately uniform across the entire surface. We found no significant hemoglobin absorbance from the smaller vessels and capillaries in these surrounding regions. Similarly, absorbance from other cytochromes in the tissue were too small to be detected. We confirmed the uniformity of the reflectance by choosing a number of different regions T for normalization, finding $<10\%$ variation in the SO₂ values calculated.

To further demonstrate the robustness of the reflectance absorbance measurement used in this study, a map of the optical path length fitting parameter, L , from Eq. 1 is shown in Fig. 6. L defines the distance that light must travel through blood. As seen in the figure, L in the vessels is roughly twice the actual vessel diameter, as expected for light that has passed downward through the vessel, reflected off the underlying tissue, and passed again through the vessel. The gradual increase in L toward the center of the vessels is also consistent with expectation. This map provides further indication that the assumptions used here to calculate SO₂ are appropriate.

To the best of our knowledge, this is the first demonstration of two-dimensional SO₂ maps generated from a single set of reflectance absorbance images. This is due, primarily, to the ability of our AOTF microscope to rapidly acquire

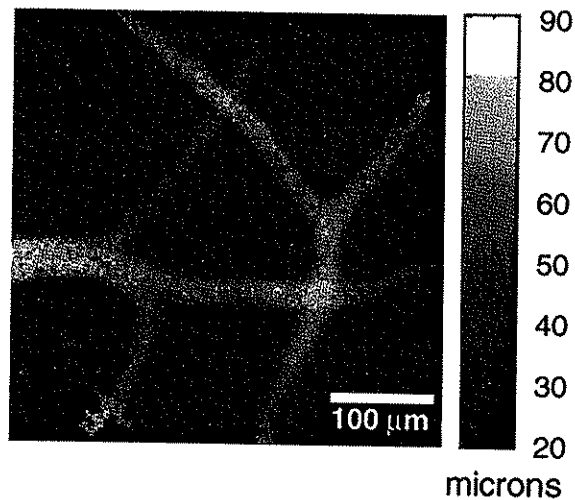


FIGURE 6 Map of the optical path length parameter L from the least-squares fitting of Eq. 1. L is the distance that the reflected light must travel through the blood and is approximately twice the vessel diameter, as expected. Actual anatomical distance is indicated by the bar in the lower right corner.

reflectance images at many different wavelengths. For the determination of SO_2 in the smaller vessels and capillaries, it will be necessary to use difference spectra, where the reflected spectra from one physiologic state are subtracted from those of another. Such an experiment can also be easily performed with our AOTF microscope.

While PO_2 has been measured within the larger pial vessels of the cerebral cortex, a capillary PO_2 measurement requires increased signal-to-noise. There are a number of ways to achieve this. First, the probe concentration in the blood can be increased. However, because the photoactivation of Pd-porphyrin compounds generates reactive oxygen species that can damage vessels, the concentration cannot be increased significantly above the 15 mg/kg currently used (Shonat et al., 1995). Second, the excitation energy and/or exposure time can be increased. While an increase in phosphorescence will result, the total amount of light delivered will also be increased. Future studies will be needed to assess how increasing the energy density and/or the exposure time will affect the measurement. The third way to improve the PO_2 measurement is to increase the total number of images used for fitting. Currently, θ_D is incremented by 60° . Decreasing this phase interval will increase the number of points available for fitting, but will also increase the light exposure and total experiment time. Finally, improvements in the AOTF crystal design and construction should increase AOTF throughput and contribute to improvements in both the PO_2 and SO_2 image quality.

Since SO_2 and PO_2 are related by the oxygen-hemoglobin dissociation curve, the nearly simultaneous generation of an SO_2 and PO_2 map quite naturally allows for an investigation of this curve in vivo with high spatial and temporal resolution. While it is known that many factors can cause this curve to shift, including pH, PCO_2 , temperature, and the

levels of 2,3-DPG, very little is known about its actual shape in the smaller vessels and capillaries where O_2 exchange takes place. Our data for pial vessels suggest that the dissociation curve may be shifted to the right of the in vitro curve published for the C57BL/6J mouse strain (Fabry et al., 1992). As such, it may be possible to have a change in SO_2 without a corresponding change in PO_2 within a region of activated neurons through a shift of the dissociation curve. If such a condition did exist, then techniques, which only measure a change in SO_2 or $[Hb]$, would incorrectly conclude that the PO_2 levels also changed. While this remains an open question, an ever-increasing number of cognitive task-activation and disease-state studies in humans, using a functional MRI technique that is sensitive to changes in deoxy-hemoglobin (BOLD), have been undertaken without a full knowledge of the underlying mechanisms (Jezzard et al., 1994; Menon et al., 1995). Because our AOTF microscope can be used to address this issue, a better understanding of these clinically relevant techniques will likely be realized.

In conclusion, we have demonstrated the use of an AOTF microscope for generating SO_2 and PO_2 maps in the cerebral cortex of mice. Because this study represents the first application of a frequency-domain technique to the measure of phosphorescence lifetime and the first demonstration of nearly simultaneous SO_2 and PO_2 maps, the versatility of the AOTF microscope for in vivo physiologic investigation is realized. Future improvements to the AOTF microscope and the imaging protocols are expected. This will likely permit a more detailed investigation of oxygen-hemoglobin binding dynamics within neuronal tissues during physiologic perturbations and increase our understanding of the complex mechanisms used to regulate the delivery of O_2 to meet the ever-changing demands of activated brain cells. In particular, the AOTF microscope may be used for metabolic studies using calcium-sensitive fluorescent dyes, as well as other functional imaging studies, which have become increasingly important in recent years for the elucidation of brain function.

This research was supported by National Institutes of Health Grants HL-40354 and HL-02847 (to A.P.K.), HL-09418-02 (to R.D.S.), and RR-03631 (to the Pittsburgh NMR Center for Biomedical Research); by a Fellowship from the W. M. Keck Center for Advanced Training in Computational Biology (to R.D.S.); by the Benjamin Franklin Technology Center of Western Pennsylvania, and by National Science Foundation Grant MCB 8920118 in support of the Science and Technology Center for Light Imaging and Biotechnology.

REFERENCES

- Adair, G. S. 1925. The hemoglobin system VI. *J. Biol. Chem.* 63:529–545.
- Bonhoeffer, T., and A. Grinvald. 1996. Optical imaging based on intrinsic signals: the methodology. *In Brain Mapping: The Methods.* A. W. Toga and J. C. Mazziotta, editors. Academic Press, San Diego, CA. 55–97.
- Chance, B., J. S. Leigh, H. Miyake, D. S. Smith, S. Nioka, R. Greenfeld, M. Finander, K. Kaufmann, W. Levy, M. Young, P. Cohen, H. Yoshioka, and R. Boretsky. 1988. Comparison of time-resolved and

- unresolved measurements of deoxyhemoglobin in brain. *Proc. Natl. Acad. Sci. USA*. 85:4971-4975.
- Fabry, M. E., R. L. Nagel, A. Pachnis, S. M. Suzuka, and F. Costantini. 1992. High expression of human β^F - and α -globins in transgenic mice: Hemoglobin composition and hematological consequences. *Proc. Natl. Acad. Sci. USA*. 89:12150-12154.
- Farkas, D. L., G. Baxter, R. L. DeBiasio, A. Gough, M. A. Nederlof, D. Pane, J. Pane, D. R. Patek, K. W. Ryan, and D. L. Taylor. 1993. Multimode light microscopy and the dynamics of molecules, cells, and tissues. *Annu. Rev. Physiol.* 55:785-817.
- Huang, C., N. S. Lajevardi, O. Tammela, A. Pastuszko, M. Delivoria-Papadopoulos, and D. F. Wilson. 1994. Relationship of extracellular dopamine in striatum of newborn piglets to cortical oxygen pressure. *Neurochem. Res.* 19:649-655.
- Jezzard, P., F. Heineman, J. Taylor, D. DesPres, H. Wen, R. S. Balaban, and R. Turner. 1994. Comparison of EPI gradient-echo contrast changes in cat brain caused by respiratory challenges with direct simultaneous evaluation of cerebral oxygenation via a cranial window. *NMR Biomed.* 7:35-44.
- Jöbsis, F. F. 1977. Noninvasive, infrared monitoring of cerebral and myocardial oxygen sufficiency and circulatory parameters. *Science*. 198:1264-1266.
- Kwong, K. K., J. W. Belliveau, D. A. Chesler, I. E. Goldberg, R. M. Weisskoff, B. P. Poncelet, D. N. Kennedy, B. E. Hoppel, M. S. Cohen, R. Turner, H. Cheng, T. J. Brady, and B. R. Rosen. 1992. Dynamic magnetic resonance imaging of human brain activity during primary sensory stimulation. *Proc. Natl. Acad. Sci. USA*. 89:5675-5679.
- Lakowicz, J. R., G. Laczko, H. Cherek, E. Gratton, and M. Limkeman. 1984. Analysis of fluorescence decay kinetics from variable-frequency phase shift and modulation data. *Biophys. J.* 46:463-477.
- Lakowicz, J. R., H. Szmajdzinski, K. Nowaczyk, K. W. Berndt, and M. Johnson. 1992. Fluorescence lifetime imaging. *Anal. Biochem.* 202:316-330.
- Lo, L., C. J. Koch, and D. F. Wilson. 1996. Calibration of oxygen-dependent quenching of the phosphorescence of Pd-meso-tetra (4-carboxyphenyl) porphine: a phosphor with general application for measuring oxygen concentration in biological systems. *Anal. Biochem.* 236:153-160.
- Malonek, D., and A. Grinvald. 1996. Interactions between electrical activity and cortical microcirculation revealed by imaging spectroscopy: implications for functional brain mapping. *Science*. 272:551-554.
- Menon, R. S., S. Ogawa, X. Hu, J. P. Strupp, P. Anderson, and K. Ugurbil. 1995. BOLD based functional MRI at 4 Tesla includes a capillary bed contribution: echo-planar imaging correlates with previous optical imaging using intrinsic signals. *Magn. Reson. Med.* 33:453-459.
- Mujumdar, R. B., L. A. Ernst, S. R. Mujumdar, C. J. Lewis, and A. S. Waggoner. 1993. Cyanine dye labeling reagents: sulfoindocyanine succinimidyl esters. *Bioconjugate Chem.* 4:105-111.
- Nair, P., W. J. Whalen, and D. G. Buerk. 1975. PO₂ of cat cerebral cortex: response to breathing N₂ and 100% O₂. *Microvasc. Res.* 9:158-165.
- Ogawa, S., T. Lee, A. S. Nayak, and P. Glynn. 1990. Oxygenation-sensitive contrast in magnetic resonance image of rodent brain at high magnetic fields. *Magn. Reson. Med.* 14:68-78.
- Ogawa, S., D. W. Tank, R. Menon, J. M. Ellermann, S.-G. Kim, H. Merkle, and K. Ugurbil. 1992. Intrinsic signal changes accompanying sensory stimulation: functional brain mapping with magnetic resonance imaging. *Proc. Natl. Acad. Sci. USA*. 89:5951-5955.
- Rosenthal, M. R., J. C. LaManna, F. F. Jöbsis, J. E. Levasseur, H. A. Kontos, and J. L. Patterson. 1976. Effects of respiratory gases on cytochrome *a* in intact cerebral cortex: is there a critical pO₂? *Brain Res.* 108:143-154.
- Rumsey, W. L., M. Pawlowski, N. Lejavardi, and D. F. Wilson. 1994. Oxygen pressure distribution in the heart in vivo and evaluation of the ischemic "border zone." *Am. J. Physiol.* 266:H1676-H1680.
- Rumsey, W. L., J. M. Vanderkooi, and D. F. Wilson. 1988. Imaging of phosphorescence: a novel method for measuring oxygen distribution in perfused tissue. *Science*. 241:1649-1651.
- Sato, N., T. Kamada, M. Shichiri, S. Kawano, H. Abe, and B. Hagihara. 1979. Measurement of hemoperfusion and oxygen sufficiency in gastric mucosa in vivo. *Gastroenterology*. 76:814-819.
- Shonat, R. D., and P. C. Johnson. 1997. Oxygen tension gradients and heterogeneity in the venous microcirculation: a phosphorescence quenching study. *Am. J. Physiol.* 272:H2233-2240.
- Shonat, R. D., K. N. Richmond, and P. C. Johnson. 1995. Phosphorescence quenching and the microcirculation: an automated, multipoint oxygen tension measuring instrument. *Rev. Sci. Instrum.* 66:5075-5084.
- Shonat, R. D., D. F. Wilson, C. E. Riva, and S. D. Cranston. 1992a. Effect of acute increases in intraocular pressure on intravascular optic nerve head oxygen tension in cats. *Invest. Ophthalmol. Vis. Sci.* 33:3174-3180.
- Shonat, R. D., D. F. Wilson, C. E. Riva, and M. Pawlowski. 1992b. Oxygen distribution in the retinal and choroidal vessels of the cat as measured by a new phosphorescence imaging method. *Applied Optics*. 31:3711-3718.
- Vanderkooi, J. M., G. Maniara, T. J. Green, and D. F. Wilson. 1987. An optical method for measurement of dioxygen concentration based upon quenching of phosphorescence. *J. Biol. Chem.* 262:5476-5482.
- Wachman, E. S., W. Niu, and D. L. Farkas. 1996. Imaging acousto-optic tunable filter with 0.35-micrometer spatial resolution. *Applied Optics* 35:5220-5226.
- Wachman, E. S., W. Niu, and D. L. Farkas. 1997. AOTF microscope for imaging with increased speed and spectral versatility. *Biophys. J.* 73:1215-1222.
- Watanabe, M., N. Harada, H. Kosaka, and T. Shiga. 1994. Intravital microreflectometry of individual pial vessels and capillary region of rat. *J. Cerebr. Blood Flow Metab.* 14:75-84.
- Wilson, D. F., and G. J. Cerniglia. 1992. Localization of tumors and evaluation of their state of oxygenation by phosphorescence imaging. *Cancer Res.* 52:3988-3993.
- Wilson, D. F., S. Gomi, A. Pastuszko, and J. H. Greenberg. 1993. Microvascular damage in the cortex of cat brain from middle cerebral artery occlusion and reperfusion. *J. Appl. Physiol.* 74:580-589.
- Wilson, D. F., A. Pastuszko, J. E. DiGiacomo, M. Pawlowski, R. Schneiderman, and M. Delivoria-Papadopoulos. 1991. Effect of hyperventilation on oxygenation of the brain cortex of newborn piglets. *J. Appl. Physiol.* 70:2691-2696.

